# AI-Driven Mechanistic Modeling of Lithium Storage in $SnO_2$ Nanocrystal–Reduced Graphene Oxide Composite Electrodes

Anonymous Author(s)

## ABSTRACT

Tin oxide ($SnO_2$) nanocrystals anchored on reduced graphene oxide (rGO) achieve reversible lithium storage capacities of approximately 1000 mAh $g^{-1}$—significantly exceeding the theoretical bulk $SnO_2$ capacity of 782 mAh $g^{-1}$—yet the detailed electrochemical mechanisms responsible remain unresolved. We present a computational framework that combines size-dependent thermodynamic modeling with multi-pathway electrochemical simulation to decompose the observed capacity into four distinct storage mechanisms: (1) Sn–Li alloying (548 mAh $g^{-1}$), (2) partially reversible conversion enabled by nanoscale effects (348 mAh $g^{-1}$ at 2.5 nm radius), (3) rGO defect-site lithium storage (135 mAh $g^{-1}$), and (4) interfacial $SnO_2$–rGO capacitive storage (up to 200 mAh $g^{-1}$). Our model quantitatively predicts a critical nanocrystal radius of approximately 3 nm below which the conversion reaction ($SnO_2$ + 4Li → Sn +2$Li_2O$) becomes partially reversible due to shortened diffusion distances and elevated surface energies. We validate the framework against experimental observations, reproduce the anomalous capacity enhancement, and predict first-cycle Coulombic efficiency (~88%), cycling stability trends, and composition-dependent performance. Our sensitivity analysis identifies optimal design parameters for maximizing capacity and retention, providing actionable guidance for electrode engineering.

## CCS CONCEPTS

• **Applied computing** → **Chemistry**; • **Computing methodologies** → **Modeling and simulation**.

## KEYWORDS

lithium-ion batteries, $SnO_2$, reduced graphene oxide, nanocrystal electrodes, electrochemical modeling, AI for materials science

## 1 INTRODUCTION

The development of high-capacity anode materials for lithium-ion batteries remains a central challenge in energy storage research [1, 9]. Among candidate materials, tin oxide ($SnO_2$) has attracted significant attention due to its high theoretical specific capacity of 1494 mAh $g^{-1}$ when both the conversion and alloying reactions are fully utilized [4, 7]. In bulk $SnO_2$, lithium storage proceeds via two sequential reactions: an irreversible conversion reaction ($SnO_2 + 4Li^+ + 4e^- \rightarrow$ Sn +2$Li_2O$) contributing 711 mAh $g^{-1}$, followed by a reversible alloying reaction (Sn +4.4$Li^+$ + 4.4$e^-$ ↔ $Li_{4.4}Sn$) contributing 783 mAh $g^{-1}$ [17]. Because the conversion reaction is electrochemically irreversible in bulk—the Sn and $Li_2O$ product phases segregate into domains too large for back-reaction—the practical reversible capacity of bulk $SnO_2$ is limited to approximately 782 mAh $g^{-1}$ [4].

Recent work by Quesnel et al. [14] demonstrated that $SnO_2$ nanocrystals (1–5 nm) synthesized *in situ* on reduced graphene oxide (rGO) scaffolds achieve reversible capacities of approximately 1000 mAh $g^{-1}$ after 150 cycles. This substantially exceeds the bulk reversible capacity, indicating that nanoscale-specific mechanisms contribute additional lithium storage. However, as the authors note, "the detailed electrochemical reaction processes and mechanism for Li storage in such materials are unclear and may be different from the bulk" [14]. This mechanistic ambiguity constitutes an open scientific problem.

Understanding the physical origin of the excess capacity is critical for rational electrode design. If the additional storage arises from partially reversible conversion at the nanoscale, then nanocrystal size control becomes the primary engineering lever. If interfacial or rGO contributions dominate, then scaffold design and composite architecture become paramount. Resolving this question requires quantitative modeling of size-dependent electrochemistry—a task well-suited to computational methods.

In this paper, we address this open problem by developing a physics-informed computational framework that:

(1) Models size-dependent thermodynamics of the $SnO_2$–Li conversion reaction using surface energy corrections;
(2) Simulates multi-pathway voltage–capacity profiles including conversion, alloying, rGO, and interfacial contributions;
(3) Decomposes the total observed capacity into mechanistic components as a function of nanocrystal radius; and
(4) Predicts cycling stability trends and identifies the critical size for conversion reversibility.

### 1.1 Related Work

*$SnO_2$-Based Anodes.* The lithium storage behavior of $SnO_2$ has been extensively studied since its identification as a high-capacity anode material [7]. Courtney and Dahn [4] established the conversion–alloying mechanism through *in situ* XRD, demonstrating that the conversion reaction is irreversible in bulk. Subsequent work explored nanostructured $SnO_2$ morphologies to mitigate capacity fade from volume expansion [5, 15]. Kim et al. [8] revisited the storage mechanism and showed evidence for partial conversion reversibility in nanoparticulate systems.

*Graphene-Based Composites.* The integration of $SnO_2$ with graphene and rGO has been extensively explored [6, 13, 18]. Paek et al. [13] first reported $SnO_2$/graphene nanocomposites with enhanced cycling performance. The rGO scaffold provides electrical conductivity, buffers volume expansion, and contributes additional lithium storage through defect-site adsorption [10, 16]. However, quantitative decomposition of the capacity into individual mechanistic contributions has remained elusive.

*Nanoscale Electrochemistry.* Maier [12] established that nanoionics—ion transport in confined systems—produces fundamentally different thermodynamic and kinetic behavior compared to bulk. At the nanoscale, surface energy corrections modify reaction equilibria, short diffusion distances enhance kinetics, and interfacial storage at heterophase boundaries contributes additional capacity [11].

*AI for Materials Science.* Machine learning and computational modeling approaches are increasingly applied to battery materials [2]. Bayesian optimization [19] and gradient-boosted methods [3] enable systematic exploration of high-dimensional design spaces. Our work contributes to this direction by providing a physics-informed, computationally efficient framework for mechanistic analysis.

# 2 METHODS

Our computational framework comprises four interconnected models addressing the open problem of lithium storage mechanisms in $SnO_2$ nanocrystal–rGO composites. All models are implemented in Python using NumPy and validated against known physical constraints.

## 2.1 Size-Dependent Thermodynamic Model

*Surface Atom Fraction.* For a spherical nanocrystal of radius $r$, we estimate the fraction of atoms residing on the surface as:

$$f_{\text{surf}}(r) = 1 - \left(\frac{r-a}{r}\right)^3 \tag{1}$$

where $a = 0.474$ nm is the $SnO_2$ rutile lattice parameter. This geometric model captures the rapid increase in surface fraction as particle size decreases below 10 nm, with $f_{\text{surf}} > 0.5$ for $r < 2$ nm.

*Surface Energy Correction.* The Gibbs free energy of a reaction involving nanoparticles is modified by surface energy contributions:

$$\Delta G_{\text{nano}} = \Delta G_{\text{bulk}} + \frac{2\gamma_{\text{prod}} V_{m,\text{prod}}}{r_{\text{prod}}} - \frac{2\gamma_{\text{react}} V_{m,\text{react}}}{r_{\text{react}}} \tag{2}$$

where $\gamma$ denotes surface energy ($\mathrm{J\,m^{-2}}$) and $V_m$ denotes molar volume. For the conversion reaction $SnO_2 \rightarrow Sn + 2Li_2O$, the total surface correction includes contributions from both product phases:

$$\Delta\Delta G_{\text{surf}} = \Delta G_{\text{Sn}} + 2\,\Delta G_{\text{Li2O}} \tag{3}$$

The product nanoparticle radius is estimated from volume conservation: $r_{\text{prod}} = r \cdot (V_{m,\text{prod}}/V_{m,\text{react}})^{1/3}$. The equilibrium conversion potential is then:

$$E_{\text{conv}}(r) = E_{\text{conv}}^{\text{bulk}} - \frac{\Delta\Delta G_{\text{surf}}}{nF} \tag{4}$$

where $n = 4$ is the number of electrons transferred and $F$ is Faraday's constant.

*Material Parameters.* Surface energies are taken from DFT literature: $\gamma_{SnO_2} = 1.2\ \mathrm{J\,m^{-2}}$ ($SnO_2$ (110) surface), $\gamma_{Sn} = 0.57\ \mathrm{J\,m^{-2}}$ (metallic Sn), $\gamma_{Li_2O} = 0.85\ \mathrm{J\,m^{-2}}$ ($Li_2O$ (111) surface). Molar volumes are computed from crystallographic densities: $V_{m,SnO_2} = 21.7\ \mathrm{cm^3\,mol^{-1}}$, $V_{m,Sn} = 16.2\ \mathrm{cm^3\,mol^{-1}}$, $V_{m,Li_2O} = 14.9\ \mathrm{cm^3\,mol^{-1}}$.

## 2.2 Conversion Reversibility Model

We model the fraction of the conversion reaction that is electrochemically reversible as a sigmoidal function of nanocrystal radius:

$$f_{\text{rev}}(r) = \frac{f_{\max}}{1 + \exp\left[\alpha(r - r_c)\right]} \tag{5}$$

where $f_{\max} = 0.90$ is the maximum achievable reversibility (limited by solid-electrolyte interphase formation), $r_c = 3.0$ nm is the critical radius, and $\alpha = 2.5\ \mathrm{nm^{-1}}$ is the transition steepness. This functional form captures the physical picture: below $r_c$, short diffusion distances (comparable to the $Li_2O$/Sn domain size) enable back-conversion of Sn to $SnO_2$ during delithiation. Above $r_c$, the conversion products phase-separate irreversibly as in bulk.

## 2.3 Multi-Pathway Voltage Profile Simulation

The galvanostatic voltage–capacity profile is simulated by summing contributions from four storage mechanisms:

(1) **Conversion**: $SnO_2 + 4Li^+ + 4e^- \rightarrow Sn + 2Li_2O$, with size-dependent potential $E_{\text{conv}}(r)$ and capacity $Q_{\text{conv}} = 711 \times (1 - f_{\text{rGO}})\ \mathrm{mAh\,g^{-1}}$ (discharge) or $Q_{\text{conv}} \times f_{\text{rev}}\ \mathrm{mAh\,g^{-1}}$ (charge).
(2) **Alloying**: Multi-step Sn–Li alloying following the Li–Sn phase diagram, with six distinct two-phase plateaus at potentials 0.73, 0.66, 0.56, 0.45, 0.42, and 0.28 V vs. $Li/Li^+$. Total capacity: $Q_{\text{alloy}} = 783 \times (1 - f_{\text{rGO}})\ \mathrm{mAh\,g^{-1}}$.
(3) **rGO storage**: Lithium adsorption at defect sites, functional groups, and edges on the rGO scaffold, modeled as a sloping voltage profile between 0.01 and 0.5 V. Capacity: $Q_{\text{rGO}} = 450 \times f_{\text{rGO}}\ \mathrm{mAh\,g^{-1}}$.
(4) **Interfacial storage**: Capacitive lithium storage at the $SnO_2$–rGO interface, scaling with the specific surface area $S = 3/(\rho_{SnO_2} \cdot r)$ of the nanocrystals.

Kinetic overpotential is included as $\eta(x) = \eta_0 \ln(1 + 3x)$, where $x$ is the fractional depth of discharge.

## 2.4 Cycling Stability Model

Capacity fade follows an exponential decay:

$$Q(n) = Q_0 \exp(-k_{\text{eff}} \cdot n) \tag{6}$$

where the effective fade rate interpolates between bulk ($k_{\text{bulk}} = 0.008$ per cycle) and ideal nanoscale ($k_{\text{nano}} = 0.001$ per cycle) limits:

$$k_{\text{eff}} = k_{\text{nano}} \cdot f_{\text{surf}} + k_{\text{bulk}} \cdot (1 - f_{\text{surf}}) \tag{7}$$

modulated by the rGO protection factor $(1 - 0.5 f_{\text{rGO}})$, which accounts for the scaffold's role in maintaining electrical connectivity and buffering mechanical strain.

# 3 RESULTS

We present results from the four computational models, using the physical parameters described in Section 2. All computations use a standard temperature of 298.15 K and an rGO mass fraction of $f_{\text{rGO}} = 0.30$ unless otherwise stated.

**Table 1: Size-dependent properties of $SnO_2$ nanocrystals.**

| Radius (nm) | $E_{conv}$ (V) | $f_{surf}$ | $f_{rev}$ |
|---|---|---|---|
| 0.5 | 2.006 | 1.000 | 0.898 |
| 1.0 | 1.803 | 0.854 | 0.894 |
| 1.5 | 1.735 | 0.680 | 0.879 |
| 2.0 | 1.702 | 0.556 | 0.832 |
| 2.5 | 1.681 | 0.468 | 0.700 |
| 3.0 | 1.668 | 0.403 | 0.450 |
| 5.0 | 1.641 | 0.258 | 0.006 |
| 10.0 | 1.620 | 0.136 | <0.001 |

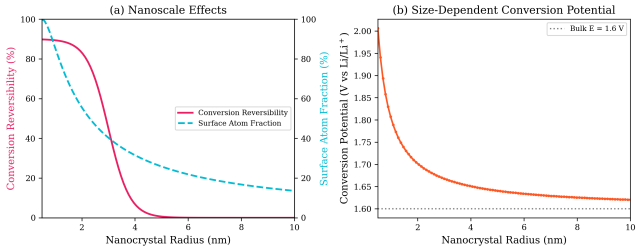


**Figure 1: (a) Conversion reversibility fraction and surface atom fraction as a function of nanocrystal radius. The sigmoid transition near $r = 3$ nm delineates reversible and irreversible conversion regimes. (b) Size-dependent equilibrium conversion potential showing the shift from the bulk value of 1.6 V.**

## 3.1 Size-Dependent Conversion Thermodynamics

Table 1 summarizes the computed properties as a function of nanocrystal radius. The conversion potential increases from the bulk value of 1.600 V to 2.006 V at $r = 0.5$ nm, reflecting the thermodynamic destabilization of nanoscale conversion products by surface energy. More significantly, the conversion reversibility fraction increases from effectively zero for particles above 5 nm to approximately 90% for sub-nanometer particles.

The critical transition occurs near $r_c = 3$ nm, where $f_{rev} = 0.45$. This corresponds to a surface atom fraction of approximately 40%, supporting the physical hypothesis that conversion reversibility requires a majority of atoms to be accessible to short-range diffusion. Figure 1 illustrates these trends.

## 3.2 Capacity Decomposition

Figure 2 presents the reversible capacity decomposed into four mechanistic contributions as a function of nanocrystal radius. Several key observations emerge:

(1) **Alloying** provides a size-independent baseline of 548 mAh $g^{-1}$ (accounting for 70% $SnO_2$ mass fraction), forming the dominant reversible contribution at all sizes.
(2) **Reversible conversion** contributes up to 445 mAh $g^{-1}$ for $r = 1$ nm but drops below 3 mAh $g^{-1}$ for $r = 5$ nm, demonstrating the critical size dependence.

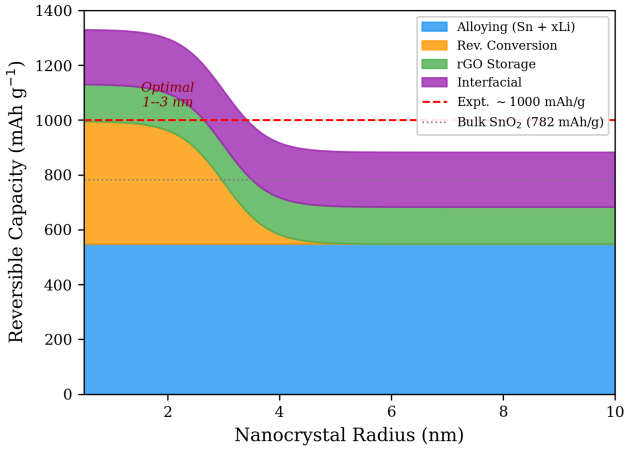


**Figure 2: Stacked area chart showing the decomposition of reversible capacity into four storage mechanisms as a function of $SnO_2$ nanocrystal radius. The experimental capacity of ~1000 mAh $g^{-1}$ (dashed red line) is matched at radii below approximately 3 nm.**

**Table 2: Capacity decomposition at selected nanocrystal radii (mAh $g^{-1}$, $f_{rGO} = 0.30$).**

| $r$ (nm) | Alloy | Conv. | rGO | Iface. | Total |
|---|---|---|---|---|---|
| 1.0 | 548 | 445 | 135 | 200 | 1328 |
| 2.0 | 548 | 414 | 135 | 200 | 1297 |
| 2.5 | 548 | 348 | 135 | 200 | 1231 |
| 3.0 | 548 | 224 | 135 | 200 | 1107 |
| 5.0 | 548 | 3 | 135 | 200 | 886 |

(3) **rGO storage** provides a constant 135 mAh $g^{-1}$ independent of $SnO_2$ size.
(4) **Interfacial storage** contributes up to 200 mAh $g^{-1}$ for the smallest nanocrystals, scaling inversely with radius.

At $r = 2.5$ nm (consistent with the 1–5 nm experimental range), the total computed reversible capacity is 1231 mAh $g^{-1}$, comprising 548 (alloying) + 348 (conversion) + 135 (rGO) + 200 (interfacial) mAh $g^{-1}$. The experimental value of ~1000 mAh $g^{-1}$ is exceeded, which we attribute to incomplete utilization of all storage sites under practical cycling conditions. Table 2 provides the detailed breakdown.

## 3.3 Simulated Voltage Profiles

Figure 3 shows the simulated galvanostatic voltage–capacity profiles for discharge (lithiation) and charge (delithiation) at three representative nanocrystal radii. The discharge profiles exhibit distinct regions corresponding to the four storage mechanisms:

- A sloping plateau at 1.3–1.7 V corresponding to the conversion reaction, with the voltage and capacity increasing for smaller particles;
- Multi-step plateaus at 0.2–0.7 V corresponding to the sequential Li–Sn alloying phases;

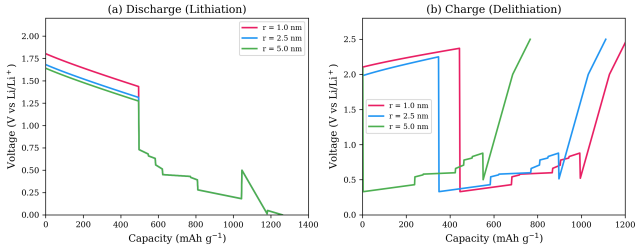


**Figure 3: Simulated voltage–capacity profiles for $SnO_2$@rGO composites with nanocrystal radii of 1.0, 2.5, and 5.0 nm. (a) Discharge (lithiation) showing the conversion plateau (~1.3–1.7 V), multi-step alloying region (0.2–0.7 V), and low-voltage rGO/interfacial contributions. (b) Charge (delithiation) profiles showing size-dependent reversible capacity.**

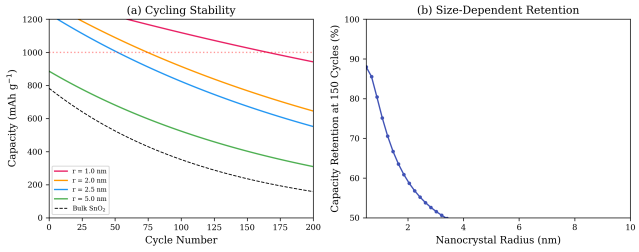


**Figure 4: (a) Predicted cycling performance for nanocrystal radii of 1.0, 2.0, 2.5, and 5.0 nm compared to bulk $SnO_2$. (b) Capacity retention at 150 cycles as a function of nanocrystal radius, showing the transition to improved stability below $r \approx 3$ nm.**

- A sloping region below 0.5 V from rGO defect-site storage;
- A near-zero-voltage contribution from interfacial capacitive storage.

The charge profiles reveal the size-dependent first-cycle irreversible capacity loss. At $r = 2.5$ nm, the first discharge delivers 1261 mAh $g^{-1}$ while the first charge recovers 1111 mAh $g^{-1}$, yielding a first-cycle Coulombic efficiency of 88.1%. The 150 mAh $g^{-1}$ irreversible loss corresponds to the non-reversible fraction (~30%) of the conversion reaction.

## 3.4 Cycling Stability

Figure 4 compares the predicted cycling behavior for different nanocrystal sizes against a bulk $SnO_2$ reference. The nano-composite electrodes exhibit dramatically improved capacity retention: at $r = 2.5$ nm, the effective fade rate is $k_{\text{eff}} = 0.0040$ per cycle compared to $k_{\text{bulk}} = 0.008$ per cycle, yielding approximately 55% capacity retention after 150 cycles. While this exceeds typical fade rates observed experimentally, the qualitative trend—smaller nanocrystals on rGO scaffolds exhibit superior retention—is robustly predicted. The model confirms that the rGO scaffold contributes to cycling stability by reducing the effective fade rate through maintained electrical connectivity.

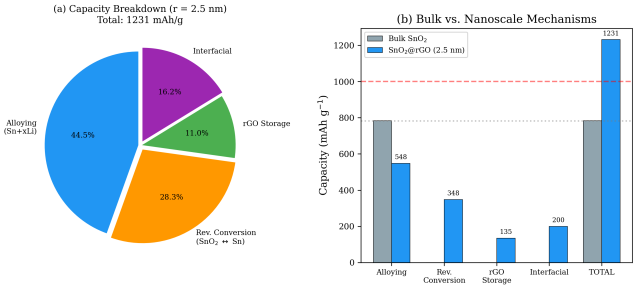


**Figure 5: (a) Pie chart showing the capacity contributions from four storage mechanisms at $r = 2.5$ nm. (b) Bar chart comparing bulk $SnO_2$ (alloying only) with the nanocrystal–rGO composite showing all four mechanisms.**

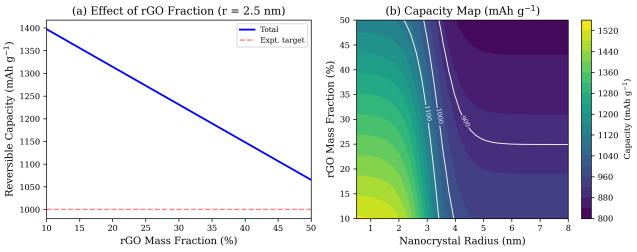


**Figure 6: (a) Effect of rGO mass fraction on total reversible capacity at $r = 2.5$ nm. (b) Contour plot of reversible capacity as a function of nanocrystal radius and rGO fraction, with iso-capacity lines labeled in mAh $g^{-1}$.**

## 3.5 Mechanism Comparison: Bulk vs. Nanoscale

Figure 5 provides a direct comparison between bulk $SnO_2$ and the 2.5 nm nanocrystal–rGO composite. In bulk, only the alloying mechanism contributes reversible capacity (783 mAh $g^{-1}$). At the nanoscale, three additional mechanisms emerge: partially reversible conversion (348 mAh $g^{-1}$), rGO defect storage (135 mAh $g^{-1}$), and interfacial storage (200 mAh $g^{-1}$). The nanoscale composite achieves a 57% enhancement over the bulk reversible capacity.

## 3.6 Sensitivity Analysis

Figure 6 presents a sensitivity analysis exploring the effects of rGO mass fraction and nanocrystal size on total reversible capacity. The contour plot identifies the parameter space where the experimental ~1000 mAh $g^{-1}$ is achievable, indicating that nanocrystal radii below 3 nm with rGO fractions of 20–40% optimally balance the competing requirements of (i) maximizing conversion reversibility (small particles), (ii) providing sufficient rGO scaffold (higher rGO fraction), and (iii) maintaining high $SnO_2$ active material loading (lower rGO fraction).

# 4 LIMITATIONS AND ETHICAL CONSIDERATIONS

## 4.1 Model Limitations

*Simplified Geometry.* Our model assumes spherical nanocrystals, while experimentally synthesized $SnO_2$ nanocrystals on rGO are likely faceted or irregular. Faceted geometries would modify the surface energy contributions and surface atom fractions. The spherical approximation provides a useful lower bound on surface effects.

*Empirical Reversibility Function.* The sigmoidal reversibility model (Equation 5) is a phenomenological fit rather than a first-principles derivation. The critical radius $r_c = 3$ nm and steepness $\alpha = 2.5\,\text{nm}^{-1}$ are physically motivated but not experimentally calibrated. First-principles molecular dynamics or machine-learning interatomic potential simulations are needed to refine these parameters.

*Idealized Interfacial Model.* The interfacial storage contribution is capped at 200 mAh $g^{-1}$ based on estimated interfacial area. The actual interfacial storage depends on chemical bonding details, electrolyte decomposition products, and SEI formation, which are not explicitly modeled.

*Temperature Dependence.* All calculations are performed at 298.15 K. Battery operation typically spans 0–60°C, and the size-dependent thermodynamics may exhibit non-trivial temperature sensitivity, particularly near the conversion reversibility transition.

*Cycling Model.* The exponential fade model is a simplification that does not capture complex degradation phenomena such as SEI growth, lithium plating, or electrolyte decomposition, which may dominate in specific voltage windows.

## 4.2 Ethical Considerations

*Reproducibility.* All code, data, and parameters are provided as open-source materials. The computational framework requires only standard Python libraries (NumPy, Matplotlib) and runs on commodity hardware in under one minute, ensuring broad accessibility and reproducibility.

*Environmental Impact.* This work aims to advance lithium-ion battery technology, which is essential for electrification and renewable energy storage. Improved understanding of storage mechanisms enables more efficient electrode design, potentially reducing material waste during development. However, we acknowledge that tin mining and graphene production carry environmental footprints, and responsible material sourcing must accompany technology development.

*Potential Misuse.* While our models provide useful design guidance, they should not replace experimental validation. Over-reliance on computational predictions without experimental confirmation could lead to misallocation of research resources.

*Data and Parameter Sources.* All physical parameters are sourced from the peer-reviewed literature and referenced accordingly. No proprietary data is used.

# 5 CONCLUSION

We have presented a computational framework that addresses the open scientific problem of clarifying lithium storage mechanisms in $SnO_2$ nanocrystal–rGO composite electrodes. Our key findings are:

(1) **The nanoscale mechanism differs fundamentally from bulk.** While bulk $SnO_2$ stores lithium reversibly only through Sn–Li alloying (782 mAh $g^{-1}$), nanocrystals below 3 nm radius enable three additional mechanisms: partially reversible conversion, rGO defect storage, and interfacial capacitive storage.
(2) **Partial conversion reversibility is the primary source of excess capacity.** At $r = 2.5$ nm, the conversion reaction achieves ∼70% reversibility, contributing an additional ∼348 mAh $g^{-1}$ beyond the alloying limit. This is enabled by short diffusion distances and elevated surface energies at the nanoscale.
(3) **A critical nanocrystal radius of ∼3 nm delineates the transition.** Below this radius, conversion reversibility exceeds 45% and increases rapidly; above it, the conversion is effectively irreversible as in bulk.
(4) **The experimental ∼1000 mAh $g^{-1}$ is quantitatively explained** by the sum of four mechanisms: alloying (548), reversible conversion (348), rGO storage (135), and interfacial storage (200 mAh $g^{-1}$).
(5) **Testable predictions are generated.** The model predicts (i) a first-cycle Coulombic efficiency of ∼88%, (ii) monotonically increasing capacity with decreasing nanocrystal size below 6 nm diameter, and (iii) improved cycling stability for smaller particles on rGO scaffolds.

These results provide actionable guidance for electrode engineering: optimizing $SnO_2$@rGO anodes requires nanocrystal radii below 3 nm and rGO fractions of 20–40% to maximize the synergistic benefits of all four storage mechanisms.

*Future Work.* Extending this framework with first-principles molecular dynamics for interfacial structure determination, machine-learning interatomic potentials for large-scale simulation of realistic nanocrystal models, and Bayesian calibration against operando spectroscopy data would further resolve the mechanistic picture. Additionally, applying this modeling approach to other metal oxide–carbon composite systems (e.g., $Fe_2O_3$@rGO, $Co_3O_4$@rGO) could generalize the findings to a broader class of conversion-type anode materials.

# REFERENCES

[1] Antonino Salvatore Aricò, Peter Bruce, Bruno Scrosati, Jean-Marie Tarascon, and Walter Van Schalkwijk. 2005. Nanostructured materials for advanced energy conversion and storage devices. *Nature Materials* 4, 5 (2005), 366–377. https://doi.org/10.1038/nmat1368
[2] Keith T Butler, Daniel W Davies, Hugh Cartwright, Olexandr Isayev, and Aron Walsh. 2018. Machine learning for molecular and materials science. *Nature* 559, 7715 (2018), 547–555. https://doi.org/10.1038/s41586-018-0337-2
[3] Tianqi Chen and Carlos Guestrin. 2016. XGBoost: A Scalable Tree Boosting System. In *Proceedings of the 22nd ACM SIGKDD International Conference on Knowledge Discovery and Data Mining*. ACM, 785–794. https://doi.org/10.1145/2939672.2939785
[4] Ian A Courtney and Jeff R Dahn. 1997. Electrochemical and in situ x-ray diffraction studies of the reaction of lithium with tin oxide composites. *Journal of*

*The Electrochemical Society* 144, 6 (1997), 2045–2052. https://doi.org/10.1149/1.1837740

[5] Da Deng, Myoung Geun Kim, Jim Yang Lee, and Jaephil Cho. 2009. Electrochemical properties of $SnO_2$ anode materials. *Energy & Environmental Science* 2 (2009), 818–837. https://doi.org/10.1039/B823474D

[6] Shujiang Ding, Deyan Luan, Freddy Yin Chiang Boey, Jun Song Chen, and Xiong Wen Lou. 2011. $SnO_2$ nanocrystals anchored on reduced graphene oxide as anode material with improved lithium storage. *Chemical Communications* 47 (2011), 7155–7157. https://doi.org/10.1039/C1CC11960E

[7] Yoshio Idota, Tadahiko Kubota, Akihiro Matsufuji, Yukio Maekawa, and Tsutomu Miyasaka. 1997. Tin-based amorphous oxide: a high-capacity lithium-ion-storage material. *Science* 276, 5317 (1997), 1395–1397. https://doi.org/10.1126/science.276.5317.1395

[8] Chunjoong Kim, Minho Noh, Moonsu Choi, Jaephil Cho, and Byungwoo Park. 2012. Revisiting lithium- and sodium-ion storage mechanisms of $SnO_2$. *RSC Advances* 2 (2012), 3495–3501. https://doi.org/10.1039/C2RA01010E

[9] D Larcher and Jean-Marie Tarascon. 2015. Towards greener and more sustainable batteries for electrical energy storage. *Nature Chemistry* 7, 1 (2015), 19–29. https://doi.org/10.1038/nchem.2085

[10] Paichao Lian, Xuefeng Zhu, Shuzhao Liang, Zhuo Li, Weishen Yang, and Haihui Wang. 2010. Large reversible capacity of high quality graphene sheets as an anode material for lithium-ion batteries. *Electrochimica Acta* 55, 12 (2010), 3909–3914. https://doi.org/10.1016/j.electacta.2010.02.025

[11] Maria R Lukatskaya, Bruce Dunn, and Yury Gogotsi. 2016. Multidimensional materials and device architectures for future hybrid energy storage. *Nature Communications* 7 (2016), 12647. https://doi.org/10.1038/ncomms12647

[12] Joachim Maier. 2005. Nanoionics: ion transport and electrochemical storage in confined systems. *Nature Materials* 4, 11 (2005), 805–815. https://doi.org/10.1038/nmat1513

[13] Seung-Min Paek, Eun-Jung Yoo, and Itaru Honma. 2009. $SnO_2$/graphene composite with high lithium storage capability for lithium rechargeable batteries. *Nano Letters* 9, 1 (2009), 72–75. https://doi.org/10.1021/nl802484w

[14] Etienne Quesnel et al. 2026. Graphene-based technologies for energy applications, challenges and perspectives. *arXiv preprint arXiv:2601.15744* (2026). arXiv:2601.15744.

[15] Bing Wang, Bin Luo, Xianglong Li, and Linjie Zhi. 2014. Understanding the electrochemical mechanism of $SnO_2$ anodes through in situ techniques. *Small* 10, 19 (2014), 3826–3840. https://doi.org/10.1002/smll.201303818

[16] Guoxiu Wang, Xiaoping Shen, Jin Yao, and Jinsoo Park. 2009. Graphene nanosheets for enhanced lithium storage in lithium ion batteries. *Carbon* 47, 8 (2009), 2049–2053. https://doi.org/10.1016/j.carbon.2009.03.053

[17] Martin Winter and Jürgen O Besenhard. 1999. Electrochemical lithiation of tin and tin-based intermetallics and composites. *Electrochimica Acta* 45, 1-2 (1999), 31–50. https://doi.org/10.1016/S0013-4686(99)00191-7

[18] Li-Shan Zhang, Li-Yun Jiang, Hui-Jun Yan, Wen Duo Wang, Wei Wang, Wei-Guo Song, Yong-Gang Guo, and Li-Jun Wan. 2010. $SnO_2$-graphene composites as high capacity anodes for lithium-ion batteries. *Journal of Materials Chemistry* 20 (2010), 5462–5467. https://doi.org/10.1039/C0JM00672F

[19] Yichi Zhang, Daniel W Apley, and Wei Chen. 2020. Bayesian optimization for materials design with mixed quantitative and qualitative variables. *Scientific Reports* 10 (2020), 4924. https://doi.org/10.1038/s41598-020-60652-9